Numerical Hurricane Prediction Using Assimilation of Remotely-Sensed Rainfall Rates

JOHN MOLINARI

Department of Atmospheric Science, State University of New York at Albany, Albany 12222

(Manuscript received 22 July 1981, in final form 2 March 1982)

ABSTRACT

Rainfall rates determined from airborne radar and infrared satellite images are combined to construct a space- and time-dependent heating function for Hurricane Anita (1977). The heating is assimilated into a three-dimensional primitive equation prediction during a 12 h pre-forecast integration, after which the heating rate is computed internally by the model. The specified heating forces initial wind and mass fields toward their observed values, and produces improved 12 and 24 h forecasts of both track and intensity compared to a control integration, for which the heating is computed internally for the entire period.

Calculations indicate that model adjustment during the period of heating can be viewed as a slow response of the vorticity field to continuous forcing of the divergence by the heating. The location and pattern of the heating relative to the center appear to be of greater importance than the magnitude of the heating. This may be of significance because remotely-sensed rainfall estimates are more likely to be accurate in the positioning of heavy rainfall than in its intensity. The initialization procedure appears capable of producing useful improvement in short-term hurricane prediction, particularly prior to landfall, when data coverage is best and accuracy is of greatest concern.

A number of authors have noted the importance of upper-level inward eddy momentum fluxes for hurricane intensification. Calculations from the simulated storm indicate that such eddy fluxes are present in Hurricane Anita and are associated in part with an anticyclonic outflow eddy over an intense local rainfall area 300 km east of the center.

1. Introduction

A major limiting factor in the success of operational primitive equation hurricane models is the lack of sufficient data to define an initial state. Even with the use of reconnaissance aircraft, it is impossible at present to collect enough quasi-synoptic data in an operational framework to allow realistic analysis of mass and wind fields at several levels near the hurricane center. In contrast, radar reflectivity and satellite infrared brightness, which are remotely sensed, are relatively easy to obtain in some detail over most or all of the storm circulation. When converted to rainfall rates, both provide an estimate of the vertical integral of condensation heating at each point. Because condensation heating is the predominant source of energy for tropical cyclones, such information is of potential value in numerical prediction, if it can be assimilated into the forecast or initial state.

Anthes (1971) specified idealized radial distributions of heating in an axisymmetric primitive equation model, and integrated to a steady-state solution. In his model, the variation of the heating rate within 100 km of the center was the major factor in the strength of the low-level wind speed maximum, while the heating outside of that radius largely controlled the intensity of the outflow circulation.

J. B. Hovermale (personal communication, 1975) investigated the value of specifying a known heating rate over 12–24 h as a dynamic initialization procedure. The heating function in his idealized simulations came from a control integration. Hovermale found that, although accurate initial winds were important at outer radii, observations of heating within 150 km of the hurricane center substantially reduced initial errors in the mass and wind fields.

In this study, dynamic initialization with a known heating field is tested in a real-data prediction of Hurricane Anita (1977). The space- and time-varying heating rates, obtained from airborne radar and satellite infrared brightness, are assimilated using a three-dimensional primitive equation model with relatively simple physical parameterizations and very fine horizontal resolution. The procedure is shown in Fig. 1. The remotely-sensed heating field is specified in the model temperature equation at each grid point during a 12 h pre-forecast integration. The 12 h period is the same chosen by Anthes (1974b) for assimilation of wind and pressure data, and is comparable to the time taken for completion of the response of wind and mass to steady heating in the study of Anthes (1971).

Following the initialization period, the specified heating is turned off, and thereafter the model is

0027-0644/82/060553-19$08.75

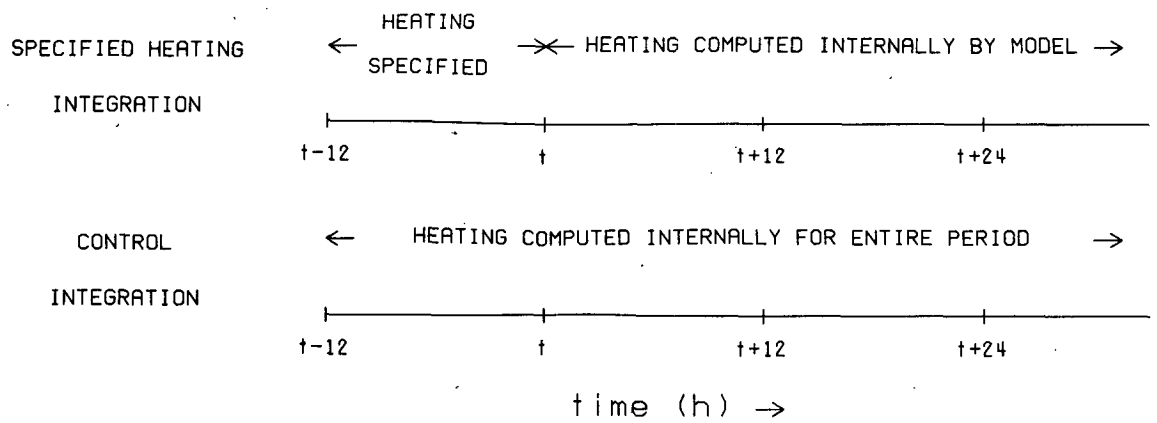

FIG. 1. Procedure for specified heating and control integrations.

allowed to compute the heating rate internally. A control integration uses internally computed heating rates during the entire period.

The primary goal of this work is to examine the potential value of this initialization procedure in improving short-term prediction of hurricane track and intensity. Calculations will be presented on the dynamics of model adjustment during the period of heating, and on the structure of the simulated storm.

2. Model description

a. Basic equations

The model utilizes the hydrostatic primitive equations in Cartesian coordinates with pressure as the vertical coordinate. The basic equations are as follows (symbols are defined in Appendix A)

$$\frac{\partial u}{\partial t} = -u\frac{\partial u}{\partial x} - v\frac{\partial u}{\partial y} - \omega\frac{\partial u}{\partial p} + fv - g\frac{\partial z}{\partial x} + \nu\nabla^2 u - g\frac{\partial \tau_x}{\partial p}, \quad (1)$$

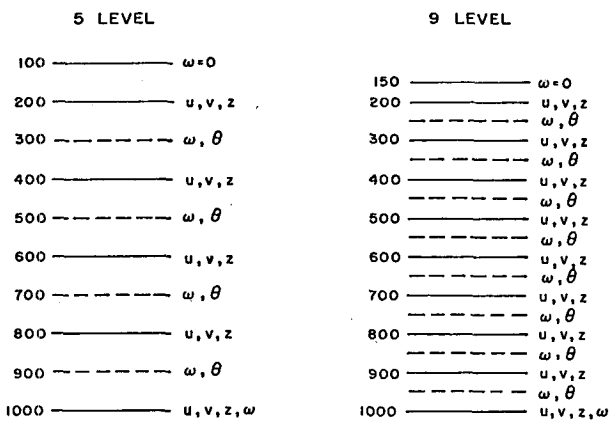

FIG. 2. Vertical structure of the 5-level and 9-level model versions.

$$\frac{\partial v}{\partial t} = -u\frac{\partial v}{\partial x} - v\frac{\partial v}{\partial y} - \omega\frac{\partial v}{\partial p} - fu - g\frac{\partial z}{\partial y} + \nu\nabla^2 v - g\frac{\partial \tau_y}{\partial p}, \quad (2)$$

$$\frac{\partial z}{\partial p} = -\frac{R\theta}{pg}\left(\frac{p}{p_0}\right)^{R/C_p}, \quad (3)$$

$$\frac{\partial \omega}{\partial p} = -\left(\frac{\partial u}{\partial x} + \frac{\partial v}{\partial y}\right), \quad (4)$$

$$\frac{\partial \theta}{\partial t} = -u\frac{\partial \theta}{\partial x} - v\frac{\partial \theta}{\partial y} - \omega\frac{\partial \theta}{\partial p} + H_L + H_R + \nu\nabla^2\theta, \quad (5)$$

$$\frac{\partial z_0}{\partial t} = -u_0\frac{\partial z_0}{\partial x} - v_0\frac{\partial z_0}{\partial y} + \frac{R\theta_0}{p_0 g}\omega_0. \quad (6)$$

b. Finite differencing procedures

The horizontal computational region extends from 87 to 97°W, and from 22 to 30°N. The horizontal grid is unstaggered and contains a uniform 0.1° latitude–longitude mesh. This fine grid was chosen to take advantage of the detail present in the radar reflectivity data.

Fig. 2a,b shows the vertical structure of the 5- and 9-level model versions used in this study. The variables are vertically staggered following Krishnamurti (1968), with u, v, and z at even levels, and ω and T at intermediate levels.

The model employs Euler-backward time differencing (Matsuno, 1966) and the "semimomentum" scheme of Shuman and Vanderman (1966) for horizontal advection, in the five-point form discussed by Grammeltvedt (1969). Upstream differencing is used for the vertical advection terms.

All other horizontal derivatives are computed using centered differences. The horizontal pressure gradient and divergence computations employ a correction procedure, proposed by Kanamitsu (1975),

which prevents the separation of solutions in space produced by centered differencing of the two terms on an unstaggered grid. The procedure has been modified slightly to produce a 3% increase in accuracy (Molinari, 1979).

c. Model physics

The model contains relatively simple formulations of physical processes. No explicit moisture cycle is present, so that the virtual temperature correction is neglected. The surface stress is evaluated bulk aerodynamically, and assumed to vanish at the top of the boundary layer, taken to be 900 mb, so that

$$-g\frac{\partial \tau_x}{\partial p} = -\frac{g}{\Delta p_{BL}}(\tau_x)_0, \tag{7}$$

$$(\tau_x)_0 = \rho_0 C_D |\mathbf{v}_0| u_0 , \tag{8}$$

with an analogous expression for the v-component equation. The drag coefficient C_D is taken as 1.5×10^{-3}, following Sundqvist (1970). Above the planetary boundary layer, upstream differencing in the vertical advection term is used to simulate the vertical diffusion process, following Rosenthal (1970).

In the horizontal diffusion term, $\nu = 1 \times 10^3$ in the 5-level integrations, and 2×10^3 in the 9-level integrations. In the 9-level integrations, for the 1000 mb wind components only, the horizontal diffusion coefficient is increased within four lines of the lateral boundaries, up to 4×10^3 one line from the boundary. No additional boundary smoothing is present.

Surface sensible heat flux is modeled implicitly by fixing the 1000 mb temperature, similar to Yamasaki (1968). Because land areas in the computational region are restricted to near the north and west boundaries, no land–ocean differences are included.

Condensation heating and radiative cooling differ in formulation during the period of specified heating and that of model-computed heating, because in the former the rainfall rate and cloud cover are known, while in the latter they must be computed or inferred. During the pre-forecast integration period, the vertical integral of the heating rate is specified using radar- and satellite-derived rainfall rates, as follows:

$$\frac{1}{g}\int_{p_t}^{p_b} \dot{Q}dp = LP. \tag{9}$$

After the pre-forecast integration, and during the entire control integration, the heating is computed by the model internally:

$$\frac{1}{g}\int_{p_t}^{p_b} \dot{Q}dp = -L\frac{\omega_b q_b}{g}. \tag{10}$$

Heating is computed whenever $\omega_b < 0$ (rising motion). The value of q_b is fixed at 18 g kg^{-1}.

Although the vertical integral of the heating is known from the rainfall rate, the vertical distribution must be specified. Syono and Yamasaki (1966) and Koss (1976) have addressed this problem in hurricane models using linear perturbation analysis on the vertically discretized primitive equations. Among the solutions are growing "quasi-balanced" modes forced by CISK-type diabatic heating which have growth rates and length scales characteristic of hurricanes. Syono and Yamasaki found particular values of a vertical partitioning parameter in their 3-layer model for which the velocity and mass perturbation structures were most like that of a hurricane. Koss (1976) noted that optimum partitioning depended on the vertical discretization in the model. The vertical distribution of heating for the "NS7 N" model of Koss, which was most similar to Fig. 2, was adopted in this study.

A general form for the diabatic heating rate per unit mass ($\dot{Q}$) at a level p is

$$\frac{1}{g}\dot{Q}(p) = \left(\frac{1}{p_b - p_t}\right)\left(\frac{\alpha(p)}{\bar{\alpha}}\right)LP, \tag{11}$$

where the overbar denotes a vertical mean, and α is a vertical partitioning parameter. In order to transfer the Koss values to the 5- and 9-level models used in this study, it is convenient to define an equivalent expression

$$\frac{1}{g}\dot{Q}(p_k) = \frac{w_k}{\Delta p_k}LP, \tag{12}$$

where k is a vertical index, and w_k is the fraction of total heating occurring in the layer between $k - \frac{1}{2}$ and $k + \frac{1}{2}$, defined by

$$w_k = \frac{\alpha_k \Delta p_k}{\bar{\alpha}(p_b - p_t)}. \tag{13}$$

The Koss values of $w_k/\Delta p_k$ were plotted at the center of the layer to which they correspond and were connected with straight lines. As a first guess, values were read directly from the Koss curve at the appropriate pressure levels of the 5- and 9-level models. For both the 5- and 9-level model versions, only slight adjustment of the first guess w_k were needed to satisfy within 0.5% both the optimum partitioning of Koss and the condition $\sum_k w_k = 1$. Fig. 3 shows the Koss vertical distribution and that of the 9-level model used in this study.

Radiative cooling is included in the model in a crude manner which is designed to simulate the storm-scale differences in cloud and cloud-free areas. During the pre-forecast period of specified heating, the extent of cloudiness is known from satellite pictures (Fig. 6). In cloudy or rainy areas, radiative cooling is set to zero. In cloud-free areas, cooling is set to 2°C day^{-1} at all levels above the surface, following Anthes (1971). During the period of internally computed heating, radiative cooling is specified

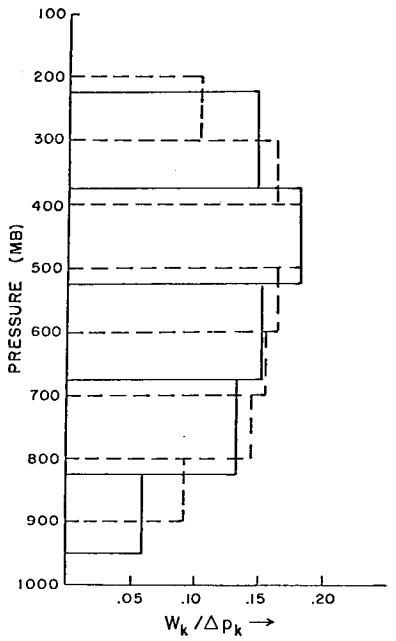

FIG. 3. Vertical distribution of the normalized percent heating in a layer for the NS7 N model of Koss (1976, solid line) and for the 9-level model in this study (dashed line). Units: fraction of total heating per 100 mb.

at all grid points which are non-precipitating, and is otherwise zero.

d. Vertical and lateral boundary conditions

Eq. 6 is an expression for the lower boundary condition of the model, following Krishnamurti *et al.* (1973):

$$w_0 = 0. \tag{14}$$

The mass continuity equation (4) is solved by integrating downward from the top model level, where $\omega = 0$. Thus the 1000 mb surface, for which ω is nonzero, acts as a free surface.

The upstream vertical differencing requires upper and lower boundary conditions on momentum and potential temperature. Vertical momentum advection is set to zero at 1000 mb for upward motion and at 200 mb for downward motion.

The boundary conditions on potential temperature are

$$\text{1000 mb: } \theta = \text{constant} = 299.65 \text{ K}, \tag{15a}$$

$$\text{100 mb (5-level model): } \theta = 362 \text{ K}, \tag{15b}$$

150 mb (9-level model):

$$\theta(150) = \theta(250) + 9. \tag{15c}$$

As noted earlier, the lower boundary condition provides a crude simulation of the effects of sensible heat transport. The upper boundary condition on temperature differs substantially in the 5- and 9-level version, due to the differences in hurricane structure in nature at 100 and 150 mb. In the 5-level model, the 100 mb potential temperature boundary condition was initially chosen to be 386 K, which is the value in both Sheets' (1969) mean Atlantic hurricane sounding and Jordan's (1958) subtropical summer mean sounding. However, adiabatic integration of the model with mechanically closed boundaries from a coarse-mesh hurricane initial state led to considerable warming of the 300 mb temperature with time. This implies that when sinking motion occurred, stability ($\partial\theta/\partial p$) was too large at the uppermost level. The problem was solved by choosing instead the mean tropopause potential temperature from Sheets' (1969) sounding, which is 24 K lower, as the 100 mb boundary condition. Physically, this can be thought of as constraining the air which sinks to the model 300 mb level to be of tropospheric origin. Adiabatic test integrations using the tropopause mean θ produced conservation of the 300 mb potential temperature over 48 h.

In the 9-level model, the upper boundary condition is applied at 150 mb. Observations show that in the layer between 150 and 200 mb, the hurricane temperature perturbation remains fairly large (e.g., see Sheets, 1969), so that a boundary condition of the form (15c) was chosen. The additive constant derives from Sheets' mean sounding.

The lateral boundary condition formulation takes on considerable importance over the relatively small 1000 × 900 km computational region. Ooyama (1969) and Rosenthal (1971) showed the necessity of having open (non-zero normal wind component) lateral boundaries over such a region. A number of approaches were tested, which are described by Molinari (1979). The most satisfactory results were produced by a form of upstream boundary conditions. On an east boundary (designated as column L), for example, for a variable q (representing u, v, θ, or z_0), define

$$\bar{u} = 0.5(u_L + u_{L-1}). \tag{16}$$

The procedure contains three conditions:

1) If $u_L > 0$,

$$\frac{\partial q_L}{\partial t} = -u_L \frac{\partial q_L}{\partial x}. \tag{17a}$$

2) If $u_L < 0$ and $\bar{u} < 0$,

$$\frac{\partial q_L}{\partial t} = 0. \tag{17b}$$

3) If $u_L < 0$ but $\bar{u} > 0$,

$$\frac{\partial q_L}{\partial t} = -\bar{u} \frac{\partial q_L}{\partial x}. \tag{17c}$$

The modification to pure upstream boundary conditions treats an inflow boundary as an outflow

boundary when $\bar{u}$ is outward, using $\bar{u}$ as the advecting velocity.

The upstream lateral boundary conditions place no explicit constraint on net inflow or outflow, and thus on total mass, in the model volume. To prevent large accumulations or deficits of mass (and thus large inflow boundary discontinuities in the 1000 mb height) from occurring, the normal component of the wind at each boundary point in the model was modified slightly each time step according to

$$v_n' = v_n + \epsilon|v_n|. \tag{18}$$

In principle, mass balance would be satisfied by

$$\epsilon = -\frac{\oint\int_p v_n dpdl}{\oint\int_p |v_n| dpdl}. \tag{19}$$

Due to the presence of the divergence adjustment procedure noted earlier (Kanamitsu, 1975), however, such an approach does not succeed (Molinari, 1979). Instead, ϵ is defined empirically as the product of a constant and

$$\bar{\omega}_0 = \frac{\int_A\int_p \nabla\cdot\mathbf{v}dpdA}{\int_A dA}, \tag{20}$$

which is an exact measure of net divergence in the volume. Such an approach does not produce exact mass balance (which may be undesirable), but always forces the model toward mass balance. The value of ϵ rarely exceeded 10^{-3} after the early part of the integration, so the actual change in the boundary normal components due to this adjustment was quite small.

The lateral boundary formulation produced sufficiently smooth forecasts that no explicit boundary smoothing was required beyond the horizontal diffusion discussed earlier. The success of this approach is undoubtedly related to the moving coordinate system (Section 2e), which allows the storm to remain near the center of the region, and may not be generally applicable to limited-area multilevel models.

e. *Moving coordinate system*

Because of the small computational region, the entire grid was allowed to move with the storm in the x and y directions with the following transformation:

$$x = x' - c_x t, \tag{21a}$$

$$y = y' - c_y t, \tag{21b}$$

where c_x and c_y are the model storm's speed of motion in the x and y directions, respectively. This transformation has the effect of replacing the horizontal advecting velocity u by $u - c_x$ and v by $v - c_y$, both in the horizontal advection terms and in the upstream lateral boundary conditions. Because the region is moving meridionally, the Coriolis parameter and Δx, both of which depend on latitude, are recomputed each time step.

To facilitate positioning of the specified heating with respect to the model storm center, c_x and c_y were allowed to vary during the integration in such a way as to keep the model storm in the center of the domain. This involved occasional jumps in c_x or c_y in one time step, making inclusion of acceleration terms in c_x and c_y somewhat difficult. To be certain that the variation of c_x and c_y with time did not distort the results, a repeat integration of one case was made with c_x and c_y constant in time, set equal to their mean values during the previous integration. The rms differences in z, u, v, and T were less than 3 m, 1 m s^{-1}, 1 m s^{-1}, and 0.1 K, respectively, and the character of the forecast fields was virtually identical.

3. Construction of the specified heating

a. *Radar data*

The National Hurricane and Experimental Meteorology Laboratory (NHEML), using airborne radar, collected data for several days during Hurricane Anita. The data used in this study were obtained from the LF (lower fuselage) C-band radar for the following times:

1808 GMT	30 August	1975
1612 GMT	31 August	1975
1718 GMT	31 August	1975
1728 GMT	31 August	1975
1810 GMT	31 August	1975
0043 GMT	2 September	1975

The data were processed by Jorgenson *et al.* (1978), using the Probert-Jones radar equation, which does not include the effects of attenuation. The data were not altered except for the one set of data collected at 500 mb, for which 9 dB(Z) was added to every point with nonzero return to correct for the effects of smaller drop sizes at higher levels (Jorgenson, personal communication, 1979). Details on the radar design and data collection can be found in Jorgenson *et al.* (1978).

The radar data were used to provide a time-dependent heating rate during the pre-forecast integration, from 1200 GMT 31 August to 0000 GMT 1 September. The four scans during that period (from 1612 to 1810 GMT) were taken at various locations relative to the storm center. It was found that, in regions of overlap of these radar observations,

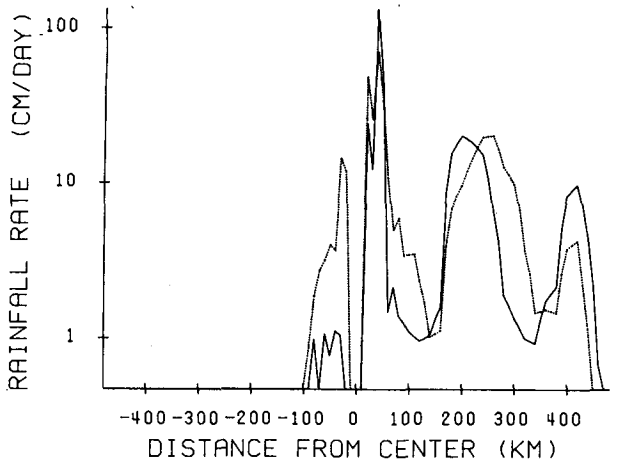

FIG. 4. East–west cross-section of the remotely-sensed rainfall rate (cm day^{-1}) at hour 0 (solid line) and hour 12 (dotted line) during the period of specified heating. The vertical axis is linear below and logarithmic above 1 cm day^{-1}.

considerable disagreement sometimes occurred. This may reflect either the large natural variability of convective features in the storm or the effects of attenuation of the 5.5 cm signal in heavy rain. Also, Jorgenson *et al.* (1978) note that, because the radar beam was elevated 2–3° (to avoid sea clutter), the beam may have been overshooting convection beyond a range of ~180 km. Coherent local time tendencies of rainfall rate could not be obtained purely from the four scans made during the 12 h period. Instead, the following procedure was adopted:

1) The six radar reflectivity (Z) maps were tabulated on a 0.05 degree latitude-longitude mesh in order to resolve small-scale details.

2) The four scans from 1612 to 1810 GMT on 31 August were composited with respect to the storm center, using at each point the Z value determined by the radar closest (in distance) to that point. The composite was assigned to 1700 GMT on 31 August.

3) Z values were converted to rainfall rates using

$$Z = 517P^{1.3} \tag{22}$$

which was determined (Willis and Spahn, 1977) using drop size distributions measured in Hurricane Eloise (1975).

4) The average rainfall rate on the 0.1 degree model grid was computed from the 0.05 degree values using

$$P'_{i',j'} = \tfrac{1}{16}[4P_{i,j} + 2(P_{i+1,j} + P_{i,j+1} + P_{i-1,j} + P_{i,j-1}) + P_{i+1,j+1} + P_{i+1,j-1} + P_{i-1,j+1} + P_{i-1,j-1}]. \tag{23}$$

Thus each point on the 10-km grid contains information from nine points tabulated on a finer grid. This procedure should considerably reduce the influence of random errors in the radar estimates.

5) At each grid point in the composite, a simple linear variation of rainfall rate in time was computed between the 1700 GMT composite and the remaining two sets of observations. The rainfall rate following the storm was produced in this manner for each 5-min segment during the 12-h pre-forecast integration.

With regard to the final step of the procedure, the rainfall rate most certainly did not vary linearly in time in nature. The storm was experiencing many short time scale convective rainfall events, including propagating spiral bands. Examination of several satellite pictures, however, indicates that the larger-scale patterns of cloudiness and precipitation in Anita were quasi-steady. Fett and Brand (1975) have noted such a slow variation of the cloudiness pattern in Pacific typhoons. Due to the relatively slow response of the velocity field in the model to changes in heating (see results), the major forcing from the heating comes from such persistent features in the rainfall pattern, and the assumed linear variation between observation times should not cause significant loss of information. The major features in the rainfall are described in Section 3c.

b. Satellite data

Due to the effects of attenuation and elevation angle of the radar beam, many convective features found relatively far from the storm center on satellite pictures were not present in the radar heating. The radar heating alone also did not allow differentiation between cloud and cloud-free areas. This knowledge was needed for specification of the simple form of longwave radiative cooling discussed previously (Section 2c).

In order to address the above problems, visible and infrared (IR) satellite images were used to supplement the radar heating function. The various shadings on IR satellite pictures were calibrated using radar-derived rainfall rates near the center, where confidence in the radar values was the highest. Using these calibrations, rainfall rates were assigned far from the center using the IR satellite pictures. The satellite-derived rainfall was merged with the radar, using only radar values inside of an approximately 120 km radius. The merged radar–satellite rainfall rates were re-interpolated in time to 5 min periods, while maintaining a smooth transition between cloud-free, cloudy, and rainy areas.

Because of the lag in response of the model wind field to the heating, the heating function was shifted six hours forward from its observation time. As a result, hour zero of the heating in Figs. 4–6 refers to 1800 GMT 31 August 1975. The procedure insures that at 0000 GMT, after 12 h of integration,

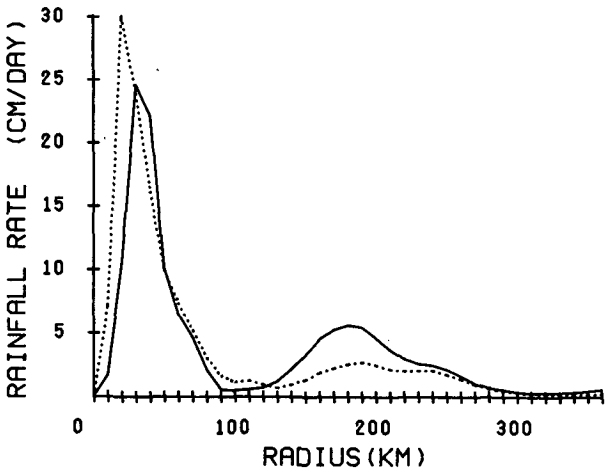

FIG. 5. Symmetric part of the specified rainfall rate (cm day^{-1}) at hour 0 (solid line) and hour 12 (dotted line) during the period of specified heating.

the wind field will have completed its response to the observed heating at the same hour. The choice of 6 h was based on the axisymmetric model results of Anthes (1971).

c. *Description of the specified heating*

Fig. 4 shows east–west cross-sections of the derived rainfall rate through the storm center at hours 0 and 12; Fig. 5 shows the average rainfall rate in each radial ring at hours 0 and 12; and Fig. 6 presents the horizontal distribution of rainfall at hour 12. Between the zero contour and the darkened outer contour in Fig. 6 is the region where satellite pictures showed cloudiness but radar calibrations indicated no rain.

Between 1800 GMT 30 August and 1800 GMT 1 September, the rainfall pattern of Hurricane Anita became progressively less asymmetric. On 30 August, all of the convection was south and east of the center. By 1800 GMT on 31 August (Fig. 4), when the storm had reached hurricane force, two separate centers of convection had developed, one associated with the storm center, the other 200 km to the southeast. The central area was still quite asymmetric, with the heaviest rain (150 cm day^{-1}) occurring in the northeast (right rear) quadrant. By 0600 GMT on 1 September, the central rain area, though maximum rainfall (80 cm day^{-1}) was still in the right rear quadrant, had become more symmetric, and the heavy rain associated with the eye wall was at a smaller radius. The outer convective area moved to almost 300 km from the center and shifted slowly counterclockwise to the east of the storm. The larger scale rainfall and cloudiness pattern remained highly asymmetric, with convection strongly suppressed north and west of the center.

The hour 0 total derived latent heating over the computational region in this study is 3.5×10^{14} W, equivalent to 1.2×10^{10} m^3 day^{-1} of rain. This value, although smaller than average for a mature hurri-

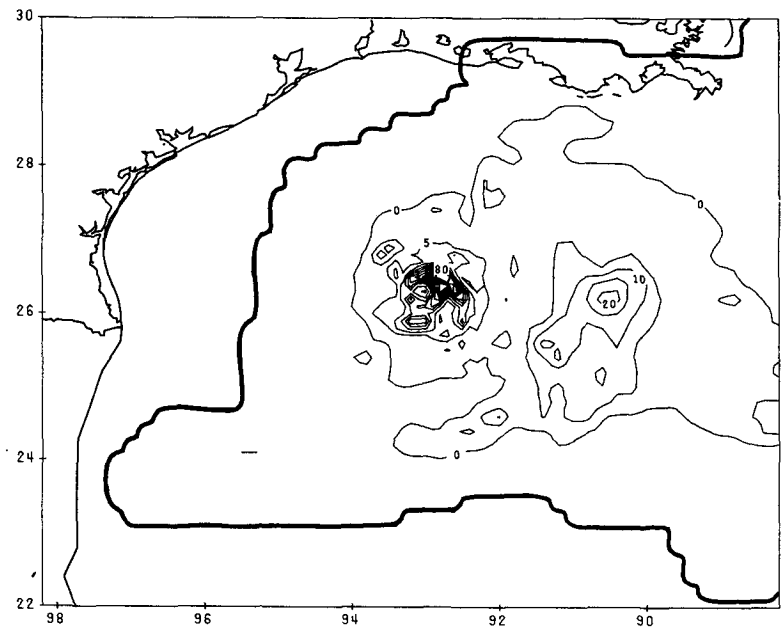

FIG. 6. Horizontal distribution of rainfall rate (cm day^{-1}) at hour 12 of the period of specified heating. In the region between the zero isopleth and the heavy outer contour, satellite pictures showed cloudiness but radar calibration indicated zero rainfall (see text for explanation).

cane, is in remarkable agreement with the 1.3×10^{10} m^3 day^{-1} of rain estimated for Anita by Griffith *et al.* (1978) using visible ATS-3 satellite images. The total heating in this study decreases slightly during the 12-h period, again in agreement with Griffith *et al.* Thus, in addition to capturing the primary features of the rainfall in Anita, the combined radar–satellite heating provides a realistic total latent energy release for the model storm.

4. Static initialization

The National Hurricane Center provided wind data from reconnaissance aircraft, and various data from other sources on microfilm. The reconnaissance data were collected near and in the storm center at several levels, but primarily at 500 m. Additional wind data were derived from conventional radiosonde reports, surface land and ship stations, and low and high cloud motion vectors. The cloud motion vectors provided an important link between the aircraft data within 150 km of the center and conventional data sources considerably further from the center.

Temperature data were not as plentiful as wind data. At the time this study was initiated, temperature data from reconnaissance aircraft were not yet processed, and large data voids existed at all levels. As a result, wind fields were analyzed, but mass fields were determined diagnostically from the wind. Wind direction and speed were analyzed at 1000, 850, 700, 500, 400 and 200 mb, and u and v components were linearly interpolated to model wind levels.

The procedure for computation of the mass fields follows Krishnamurti (1969), except in the streamfunction boundary conditions, which will be discussed later. The streamfunction is computed at each level by solving

$$\nabla^2\psi = \zeta, \tag{24}$$

where ζ is the relative vorticity computed from u and v. Using this streamfunction, the height field at each level is derived from relaxation of the reverse balance equation

$$\nabla^2 z = \frac{f}{g}\nabla^2\psi + \frac{\beta}{g}\frac{\partial\psi}{\partial y} - \frac{2}{g}J\left(-\frac{\partial\psi}{\partial y}, \frac{\partial\psi}{\partial x}\right), \tag{25}$$

using geostrophic boundary conditions

$$z = \frac{f}{g}\psi. \tag{26}$$

The potential temperature at intermediate levels is determined by integrating the hydrostatic equation (3) layer by layer.

The streamfunction calculation plays an essential role in the above procedure. To solve (24), boundary conditions on ψ must be such that the net rotational flow normal to the boundaries vanishes at each level. Many techniques have been proposed to solve (24) which vary primarily in the way the boundary normal wind component is adjusted. In a hurricane over a limited area, the net divergence in the inflow and outflow layers can be very large, and the boundary flow can become distorted by the boundary condition calculation, with accompanying interior distortions in the streamfunction, and thus in the height and temperature fields. In this study, such a problem occurred, particularly at 200 mb (Molinari, 1979). After testing several procedures, the best results were obtained by linearly extrapolating the boundary values of u and v to zero at an outer boundary 50 grid points away, carrying out the relaxation over the large region with homogeneous boundary conditions, and extracting ψ over the original region from the homogeneous solution at each level. These streamfunction values were used in (25) to determine the initial mass field.

Analyzed winds were used directly in the initial state. The analyzed winds were found superior to a velocity field reconstructed from rotational and divergent components (Molinari, 1979). Hoke and Anthes (1977) also found this to be true in a numerical hurricane prediction on a 60 km grid. In both cases, a more extensive than normal data base probably played a significant role. Because the mass tends to adjust to the wind in hurricane-scale features (Washington, 1964), the effect of errors in the derived initial mass field are likely to be minimized by the initial observed winds.

5. Results of integrations

a. Initial experiments with a Pacific typhoon

The initial experiments using the multilevel model dealt with Typhoon Wendy (1968), a storm travelling rapidly (11 m s^{-1}) westward in the South China Sea. The radar data for the storm were obtained from PPI photographs from the Hong Kong radar and were thus uncorrected for distance from the radar and various other effects. Rainfall intensity at points of non-zero return was defined simply as a function of radius because digitized reflectivity values were unavailable. In addition, reconnaissance aircraft data were sparse and limited to one level, making initial analysis difficult. When the extensive digitized radar and reconnaissance data from Hurricane Anita became available, it was chosen for the central case study of this work. Nevertheless, the typhoon case study provided an extreme test of the procedure and the initial results are worth examining.

During the early part of the integration, the divergent part of the wind responded extremely rapidly to the large specified heating rate. As a result, despite 300°C day^{-1} condensation heating at some grid points, large upward vertical motions with associated adiabatic cooling quickly developed (within 10 time

steps, less than 3 min), and the local time change of potential temperature was the small difference between these large effects.

The response of the rotational wind was considerably slower. This was not unexpected from geostrophic adjustment theory, which predicts a mass to velocity adjustment, because specifying the heating is in some respects like perturbing the mass field. The model storm moved at 4 m s^{-1}, less than half the observed speed, owing to inaccuracies in the initial low-level wind analysis, for which little data were available. Meanwhile the heating function, specified using the observed storm motion, became horizontally decoupled from the storm circulation. After only one hour of integration, the circulation center of the model storm was 20 km (two grid points) east of the center of specified heating. Continued integration led to a complete decoupling, with the primary circulation to the east, and a weaker cyclonic circulation developing underneath the fast-moving specified heating function to the west. These early results with a fast-moving typhoon indicate that under extreme conditions, when the initial state is very inaccurate, the specified heating and the model storm can become decoupled before there is time for them to interact.

A fundamental change in procedure was required to solve this problem. In subsequent integrations, the remotely-sensed heating field was defined with respect to the storm center, and positioned to follow the model storm track, not the observed track. This procedure insured that the specified heating would have time to produce a response in the model mass and velocity fields. The nature of this response is described in Section 5c.

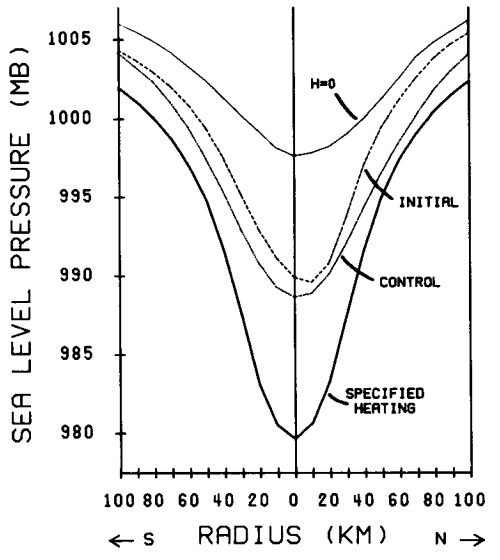

FIG. 7. North–south profile of sea-level pressure (mb) at hour 12 for the specified heating integration (dark solid line); control integration (dotted line); initial state value (dashed line); and zero heating integration (light solid line).

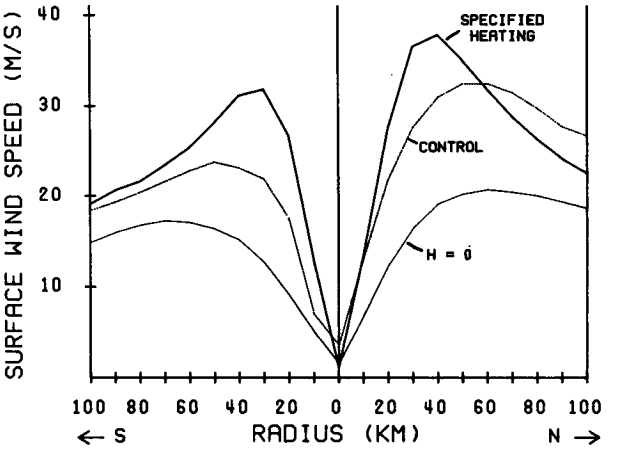

FIG. 8. North–south profile of surface wind speed (m s^{-1}) at hour 12 for the specified heating integration (dark solid line); control integration (dotted line); and zero heating integration (light solid line).

Given the lag in response of the wind field, the specified heating field was shifted forward in time by 6 h, so that the hour 0 value of the heating corresponded to 1800 GMT 31 August. The choice of 6 h was based on the time taken in the axisymmetric model of Anthes (1971) for the storm inner area to complete its response to idealized steady heating. The above two procedures were applied to the Hurricane Anita case study.

b. Hurricane Anita case: comparison of specified heating and control integrations

In Figs. 7 and 8, the specified heating and control integrations are compared at hour 12. The two start from an identical initial state and differ only in the heating function. The procedure for computing the heating rate in the control integration contains the essential characteristic of the majority of more sophisticated approaches in hurricane models: that the rainfall rate at a point be proportional to the latent energy supplied by the grid-scale winds. Any approach that uses moisture convergence to determine rainfall, no matter how sophisticated, cannot match the initial observed rainfall, to the extent that errors exist in the initial winds. These errors influence not only the computed heating at time zero, but the evolution of the heating field thereafter, and thus the evolution of the wind and mass fields in the model storm. The control integration provides a measure of the influence of errors in the initial state on forecast accuracy, and the differences between it and the specified heating integration measure to what extent the known heating reduces such errors.

Fig. 7 shows a north–south cross-section of surface

TABLE 1. Errors in predicted storm track (km) for the specified heating and control integrations. Values would be roughly half as large in nautical miles, the most commonly used unit for such errors.

	East-west error		North-south error		Vector error	
Hour	Specified heating	Control	Specified heating	Control	Specified heating	Control
12	30	100	44	44	53	109
24	50	160	121	121	131	201
36	50	200	149	143	157	246

pressure through the storm center for the specified heating and control integrations, and for an integration in which heating was set to zero. The specified heating produced a minimum central pressure of 979.6 mb, very close to the observed 0000 GMT 1 September value of 979 mb (Lawrence, 1978), even though the initial nonlinear balanced central pressure was 990 mb, 4 mb above that observed. The radial pressure gradient at hour 12 was much larger than its initial value.

The control integration produced a slowly deepening storm after initial filling, and at hour 12 had a minimum central pressure of 989 mb, 10 mb higher than observed. Thus, starting from the same initial state, the specified heating integration developed a structure much closer to observations than the control experiment. In the zero heating integration, the model storm filled to 998 mb in 12 hours.

Fig. 8 shows the accompanying hour 12 wind speeds. The integration with specified heating performed closest to observations, which showed a maximum speed of $\sim$45 m s^{-1}. The control integration contained a diffuse and weaker (31 m s^{-1}) maximum wind speed. The zero heating integration weakened to 19 m s^{-1}.

The differences in the predictions were not caused by an underestimate of the rainfall rate in the control integration. In fact, the total heating in the control integration was greater than that of the specified heating case throughout the 12 h initialization period, and the maximum point values were comparable. The fundamental difference occurred in the location and pattern of the heating. The control integration maintained maximum heat release in the right front quadrant of the storm while the observations in the specified heating integration showed heating to be greatest in the right rear quadrant. Large heating rates extended further from the center in the control and the radial gradient of heating was smaller. The more realistic storm intensity in the specified heating integration suggests that the pattern (i.e., ∇^2) and location of the heating with respect to the center play a more important role than the intensity of the heating. This result is encouraging, because although errors are known to exist in radar and satellite rainfall estimates, the positioning of the major features should be reasonably accurate.

Figs. 7 and 8 indicate that assimilation of remotely-sensed heating rates can produce a superior initial state. The value of this must be measured by the retention of such improvement after the known heating has been turned off. Table 1 shows errors in predicted storm track (in km) at and beyond hour 12, when the heating rate was computed internally in both integrations. As noted earlier, the storm remained near the center of the computational region in each integration, and the track was determined from the mean speed of motion of the region over the 12 h period. The most significant differences occurred in the prediction of westward motion. Both integrations predicted faster than observed westward motion, but the specified heating integration had only a 50 km error after 36 h, compared to 200 km in the control. In addition, if the errors are compared only after the specified heating was stopped, the east-west error was only one fifth of that of the control integration. Although both equally underestimated the southward motion, the vector error was smaller in the integration using the specified heating. The results shown in Table 1 indicate that improvements in the initial state due to the specified heating were retained in the prediction of storm motion once the heating was turned off.

The intensity predictions at hour 36 were also closer to observations in the specified heating integration. In nature, the storm rapidly deepened between hours 24 and 36. The relatively simple physics in this model was not able to simulate the rapid deepening. Nevertheless, the specified heating integration retained a minimum surface pressure 7 mb lower, a maximum surface wind speed 5 m s^{-1} larger and a more realistic radial variation of wind speed than the control at hour 36. In addition, the largest predicted rainfall rate was 80 cm day^{-1} north of the center, closer in position and intensity to the observed value of 100 cm day^{-1} than in the control integration, which had a maximum rainfall rate of less than 60 cm day^{-1}. These improvements occurred despite the fact that the rms differences in the various forecast fields were slightly smaller at hour 36 than at hour 12. This slow approach toward a control integration was also found in an axisymmetric model by Hoke (1976), who attributed it to the dominance of both lateral boundary forcing and implicit constant forcing from the ocean. In this study, use of the moving coordinate system which maintained each storm near the center of the region despite differences in speed of motion, and specification of a constant vertical heating distribution for both cases, also tended to force the integration slowly toward the control. An explicit moisture cycle and larger computational region will be incorporated into the model to reduce such constraints. Nevertheless, the comparisons show

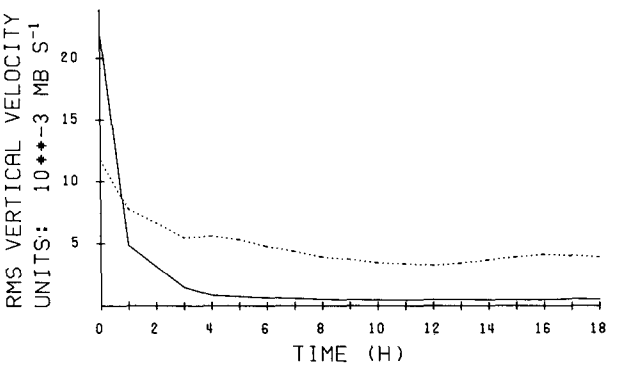

FIG. 9. Root-mean-square values of vertical velocity (mb s^{-1}) during and for six hours after the period of specified heating at 1000 mb (solid line) and 500 mb (dashed line).

that even with these constraints, predicted track and intensity were closer to observations in the specified heating integration throughout the 36 h period.

c. *Model adjustment during the period of specified heating*

Fig. 9 shows the rms values of vertical velocity ω at 1000 and 500 mb during the first 18 h of integration. The former is an approximate measure of external and the latter of internal gravity wave activity. Both decreased substantially from their unbalanced initial values to stable values by the end of the period of specified heating, indicating that the model storm adjusted to the intense heating without developing large imbalances. In addition, the jump in ω values present when the specified heating was turned off disappears by hour 13, and the integration proceeds with no significant increase in noise.

The adjustment process was investigated using the vorticity equation. Fig. 10 shows the rms difference in surface vorticity between the specified heating and control integrations over 49 points centered on the storm. The vorticity difference slowly but steadily expanded during the initialization period.

The two leading terms in the vorticity equation at the surface in both integrations were the divergence and horizontal advection terms. To investigate the reasons for the more accurate track forecast in the specified heating case, the algebraic mean value for each term over a 1.2 degree latitude–longitude area directly east of the center was subtracted from the mean value for an identical area to the west. The result indicates the role of each term in the predicted track, with positive values indicating westward motion.

Fig. 11 shows the variation of the sum of the two terms at the surface during the period of heating. During the first two hours of model adjustment, the instantaneous values were unrepresentative of hourly means and were not plotted. The graph confirms the

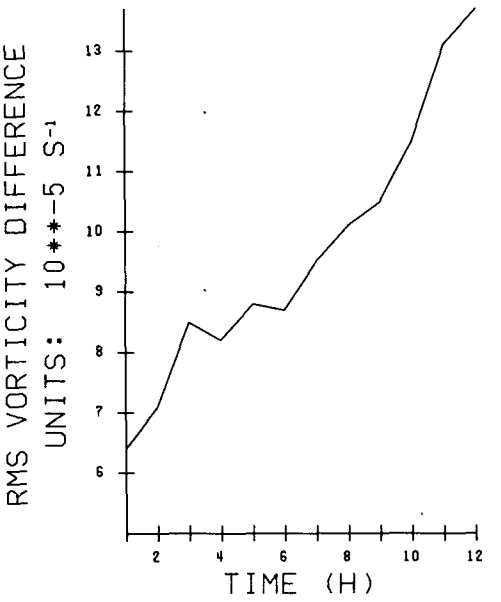

FIG. 10. Root-mean-square difference in vorticity (s^{-1}), over 49 grid points centered on the storm, between the specified heating and control integrations.

results shown in Table 1, that the control integration moved the storm too rapidly westward, while the specified heating integration moved much more slowly westward, as was observed.

Table 2 shows the individual variations of the two leading terms. Both terms, with little exception, contributed to the westward motion of the storm. As the specified heating became more symmetric, the divergence term acted to increase and the vorticity advection to decrease westward motion from its in-

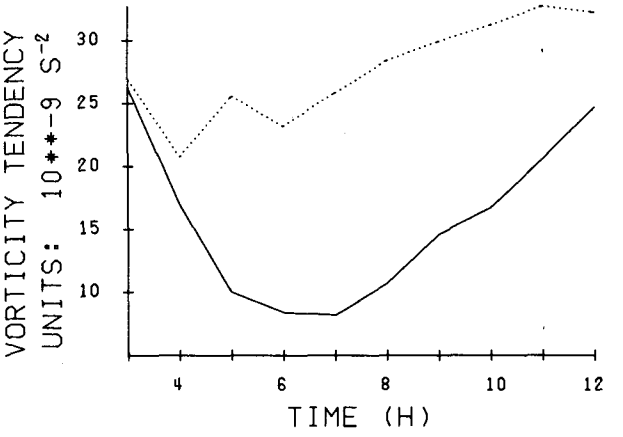

FIG. 11. Mean value of the sum of the horizontal advection and divergence terms of the vorticity equation over a 1.2 degree latitude–longitude area west of the storm, minus the mean value of the sum over an identical area to the east, for the specified heating integration (solid line) and the control (dashed line). Positive values of the resultant tendency indicate westward motion of the storm.

TABLE 2. Time variation of the divergence and horizontal advection terms in the vorticity equation for the specified heating and control integrations (units: 10^{-9} s^{-2}). Each number represents the mean value over a 1.2 degree latitude-longitude region directly west of the center minus the mean for an identical area east of the center. Positive values indicate that the term acting alone will move the storm westward.

	Divergence term		Advection term	
Hour	Specified heating	Control	Specified heating	Control
2	5.0	10.4	29.5	34.5
3	6.6	3.7	19.7	23.3
4	3.7	−6.8	13.3	27.6
5	1.0	1.0	9.0	24.6
6	1.8	7.0	6.6	16.2
7	2.6	5.4	5.6	20.5
8	6.2	5.9	4.5	22.5
9	8.9	4.7	5.7	25.3
10	11.0	4.0	5.7	27.2
11	15.4	3.4	5.2	29.3
12	18.4	5.5	6.3	26.8

itial value. The control integration maintained the large initial state vorticity advection and thus the erroneously rapid westward motion. The steady decrease of the vorticity advection in the specified heating integration can be interpreted in terms of the rapid response of the divergence, because in the friction layer the vorticity advection by the divergent wind component is significant as air flows inward across vorticity lines. At 600 mb (not shown), where divergence is small, the vorticity advection term diverged slowly from the control, in the manner of Fig. 10. The data support the view that adjustment to the heating occurred in the vorticity field as a slow response to continuous forcing of the divergent component.

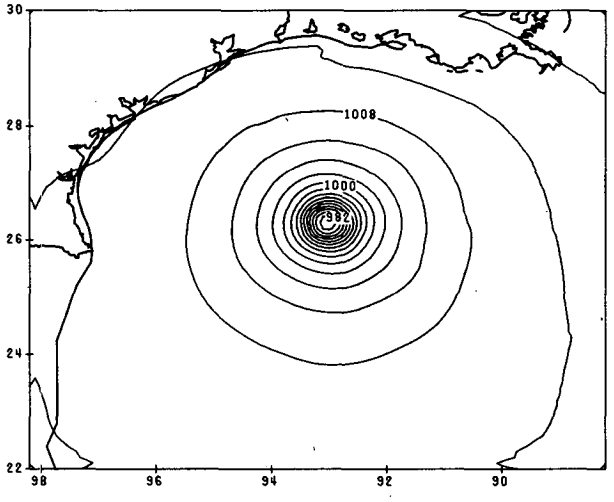

FIG. 12. Surface pressure (mb) for hour 12 of the 9-level simulation.

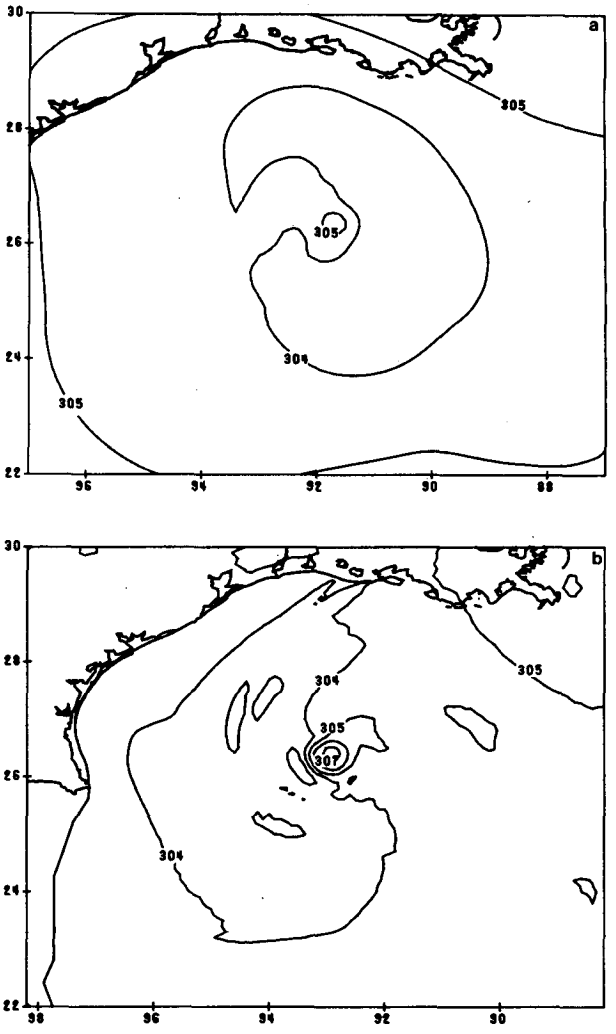

FIG. 13. Potential temperature at 850 mb in the 9-level simulation for (a) the initial state and (b) hour 12 of the specified heating.

The comments in this section are not meant to imply that the model storm can entirely adjust to the heating in 12 h. Given the speed of response of the rotational wind and the continuing evolution of the large scale, this is unlikely to occur. Rather, the model response to 12 h of forcing by the known heating rate was sufficient to produce and maintain an improvement over the control integration in the prediction of hurricane track and intensity.

d. Nine-level simulation

Pfeffer (1958) noted the importance of azimuthal asymmetries of the wind in the maintenance of tropical cyclones. In the present study, the role of asymmetries associated with the strongly asymmetric heating was investigated. For this purpose, the model was integrated with greater vertical resolution for 12 h using the specified heating. The storm track was

nearly identical to the five-level track described earlier. Figs. 12–16 show the surface pressure field at hour 12 and the initial and hour 12 potential temperature fields at selected levels. The coastline has been shifted to indicate the motion of the storm. The pressure field was nearly symmetric and contained an eye and eye-wall feature, but no significant perturbation accompanied the outer rain area. In the potential temperature fields, again no significant feature existed east of the center. In that region, any warming generated by condensation heating was quickly advected away, in contrast to the hurricane core, where sharp temperature gradients developed.

The wind fields at 1000, 600 and 200 mb are shown in Figs. 17–19. At low and middle levels, no strong asymmetries were apparent. At 200 mb, however, a significant anticyclonic outflow anomaly developed. Outflow layer observations of Hurricane Anita are available from cloud motion vectors at 1600 GMT on 31 August and 1 September (Rodgers *et al.*, 1979). Unfortunately, neither of these observations falls within 8 hours of 0000 GMT 1 September, when Fig. 19 is valid. Nevertheless, these observations show that although outflow was apparently underestimated in the northeast quadrant, strong anticyclonic diffluence did exist over the eastern rainy area. The lack of westerlies predicted south of the storm center at 200 mb cannot be verified, because even the high-resolution vectors cannot always provide information close to the center, where identifiable bright areas often move with the low-level winds (Rodgers *et al.*, 1979).

A crucial process in the intensification of tropical cyclones is the lateral flux of angular momentum from the storm environment. With the exception of a small term involving the variation of the Coriolis parameter, which usually tends to weaken storms (Frank, 1977), only the lateral flux process can supply momentum to the hurricane volume to offset frictional losses (Anthes, 1974a). In particular, large

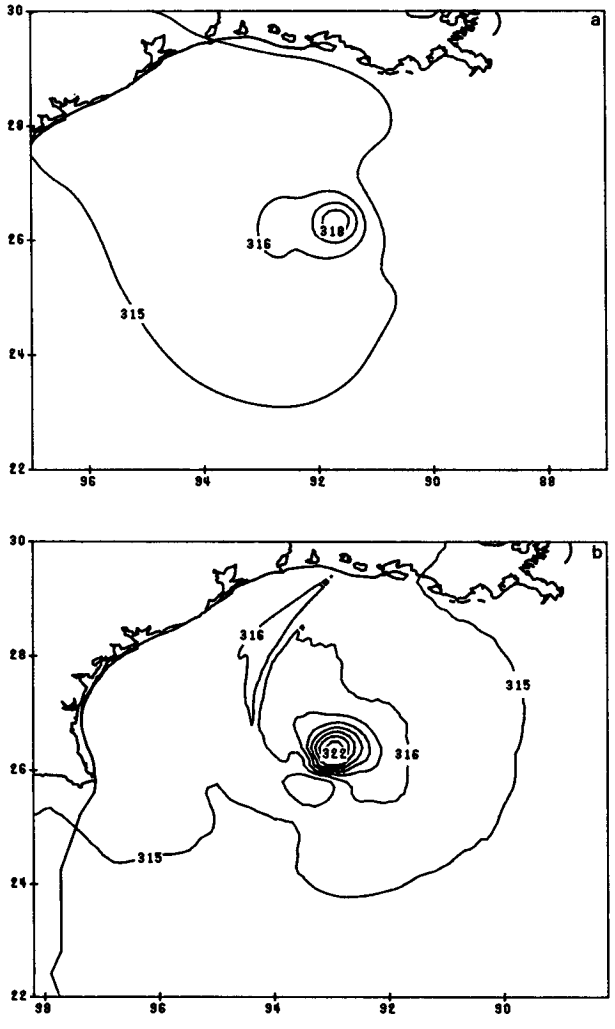

FIG. 14. As in Fig. 13, but for 650 mb.

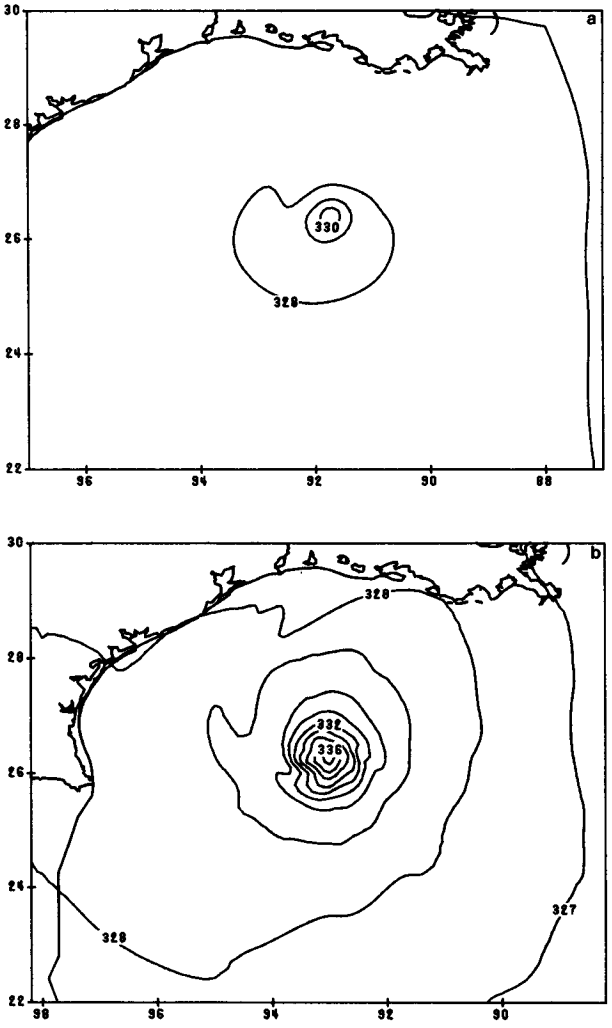

FIG. 15. As in Fig. 13, but for 450 mb.

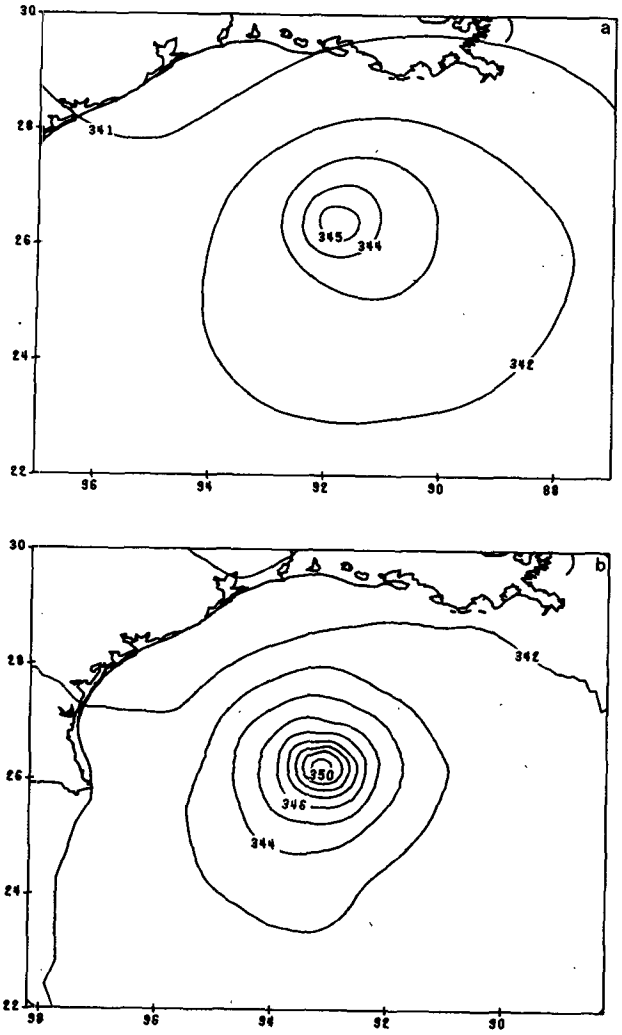

FIG. 16. As in Fig. 13, but for 250 mb.

import of angular momentum by horizontal eddies at upper levels has been found to be essential to hurricane development, both in observational studies (Palmén and Riehl, 1957; Pfeffer, 1958; Black and Anthes, 1971) and in a numerical study (Pfeffer and Challa, 1981). Previous observational studies have relied primarily on radiosonde data and cloud motion vectors, and generally cannot provide reliable calculations within 200 km of the center. In the present study, high-resolution wind fields from model output are available within 360 km of the center at several levels. Of particular interest is the relationship of the asymmetric heating distribution to the development of the storm.

The lateral momentum flux term at radius r_1 can be written

$$\left.\frac{\partial M}{\partial t}\right)_{\text{L.F.}} = -\frac{2\pi}{g}\int_{p_2}^{p_1} r_1^2(\bar{v}_\lambda\bar{v}_r + \overline{v'_\lambda v'_r})dp, \quad (27)$$

where

$$\bar{x} = \frac{1}{2\pi}\oint x d\lambda, \quad x' = x - \bar{x}.$$

The terms in (27) were computed after bilinearly interpolating u and v to cylindrical coordinates using Δr = 10 km and $\Delta\lambda$ = 15°, and computing v_r and v_λ at each point. Fig. 20 shows the mean lateral flux term as a function of radius for various layers. At these relatively small radii, cyclonic inflow supplied momentum at low levels and cyclonic outflow carried it away at upper levels, with a positive net contribution by the mean flow. Fig. 21 shows the eddy fluxes. The total eddy flux opposed the mean at these radii. Outside of the 250 km radius, however, a strong eddy flux convergence was present, produced primarily by a large inward eddy flux at 200 mb (Fig. 21c), which occurred at and outside of the radius of the outer rainfall maximum. To obtain a better physical understanding of this striking feature in the outflow layer, the azimuthal variations of the "local" eddy flux, $r^2v'_rv'_\lambda$, were examined. Large positive contributions occurred in the anticyclonic outflow region associated with the outer rainfall maximum, and west of the center where outflow interacted with northerlies associated with a synoptic-scale anticyclone to the west. Although it is not possible to determine cause and effect, the evidence suggests that a strongly asymmetric rainfall distribution at radii well-removed from the center (250–300 km in this case) is associated with the large inward momentum fluxes often observed in intensifying storms.

6. Summary and conclusions

A heating field constructed from remotely-sensed rainfall rates was specified during a 12-h pre-forecast integration, after which the heating was computed internally in the model. The specified heating forced the model wind and mass fields toward an initial state close to that observed, and produced improved 12- and 24 h forecasts of both track and intensity compared to a control integration, for which the heating was computed internally during the entire period.

At the start of the integration, the vertical motion, and thus the divergent component of the wind, responded rapidly to the heating, while the vorticity field responded more slowly. The latter is expected from linear theory (Washington, 1964), because specifying the heating is similar to perturbing the mass field. In order to allow time for the vortex to become coupled with the heating, it was necessary to design the heating field to follow the storm center in the model rather than its position in nature. Once this process was incorporated, the model storm approached the structure observed. The improvement in track achieved after the initialization period

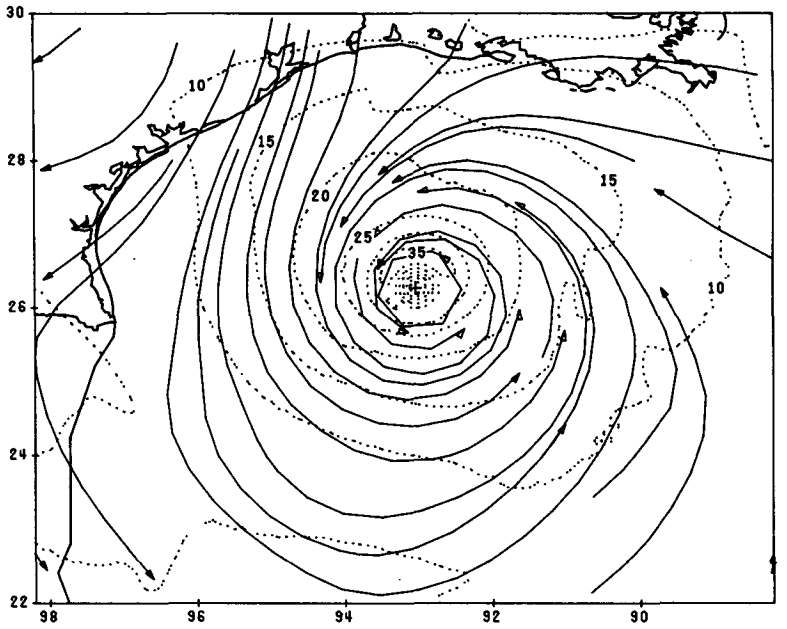

FIG. 17. Wind at 1000 mb for hour 12 of the 9-level simulation.

evolved primarily through a reduction in low-level vorticity advection forced by the specified heating, while the control integration maintained the erroneously large value present initially.

The location and pattern of the heating was found to be more important in determining storm track and intensity than the absolute magnitude of the heating. Because remotely-sensed rainfall rates are more likely to be accurate in location than magnitude, this is an encouraging result.

The role of the strongly asymmetric heating distribution in the maintenance of the storm circulation was investigated in terms of lateral fluxes of relative angular momentum. Many authors (e.g., Palmén and Riehl, 1957; Pfeffer and Challa, 1981) have noted the importance to hurricane development of inward

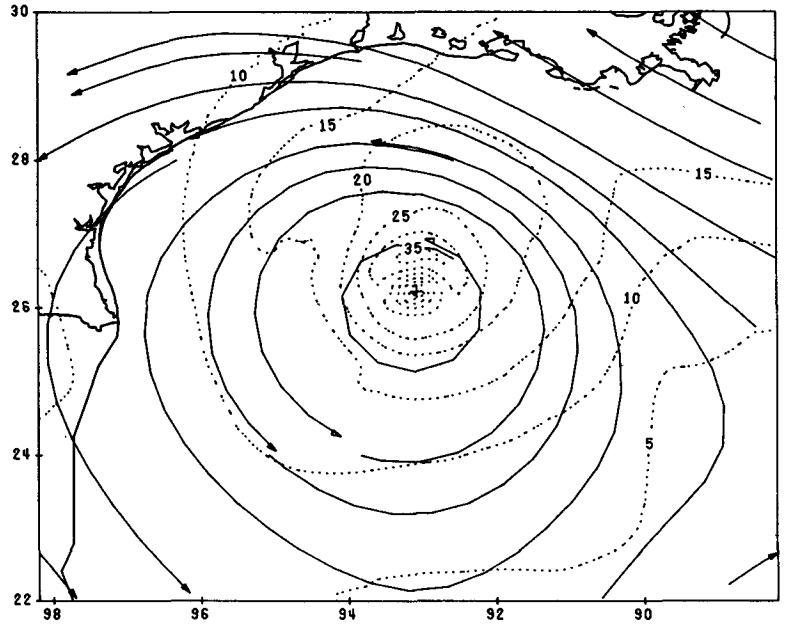

FIG. 18. As in Fig. 17, but for 600 mb.

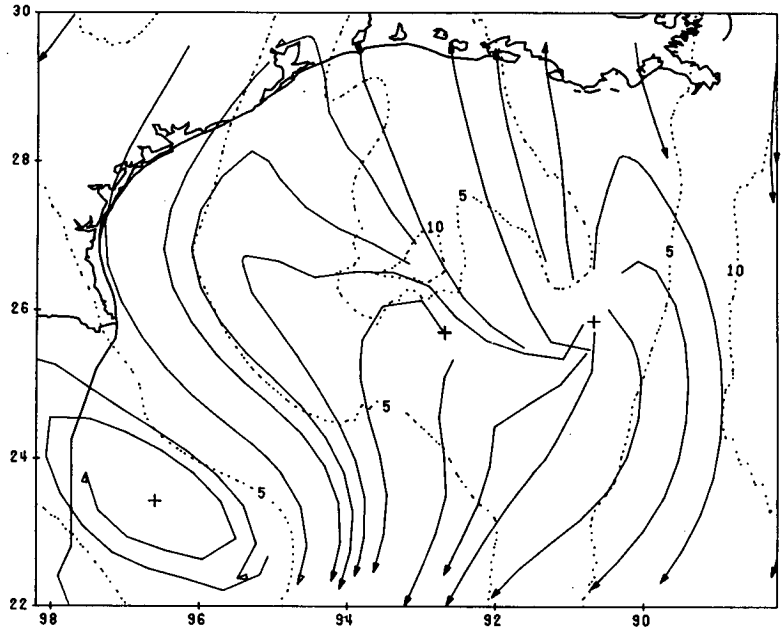

FIG. 19. As in Fig. 17, but for 200 mb.

eddy momentum fluxes at upper levels. In this study, large inward eddy momentum fluxes at 200 mb were associated in part with an anticyclonic outflow eddy over the outer rainfall maximum (Fig. 6). The results suggest that the presence of a localized region of heavy rainfall well outside of the central rain area can contribute to the inward eddy fluxes often seen in intensifying tropical storms.

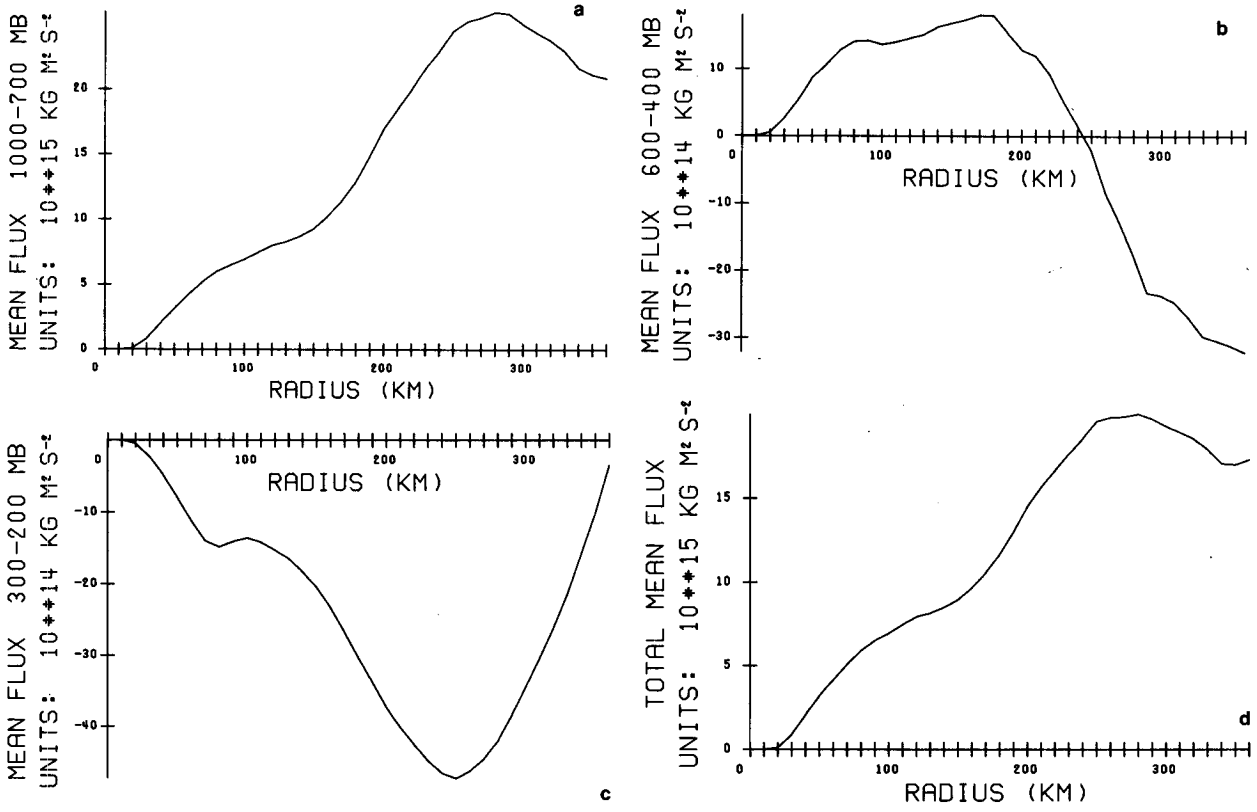

FIG. 20. Contribution of the mean lateral flux term to the time change of momentum (kg m^2 s^{-2}) plotted as a function of radius for (a) 1000–700 mb layer; (b) 600–400 mb; (c) 300–200 mb; and (d) total vertical integral.

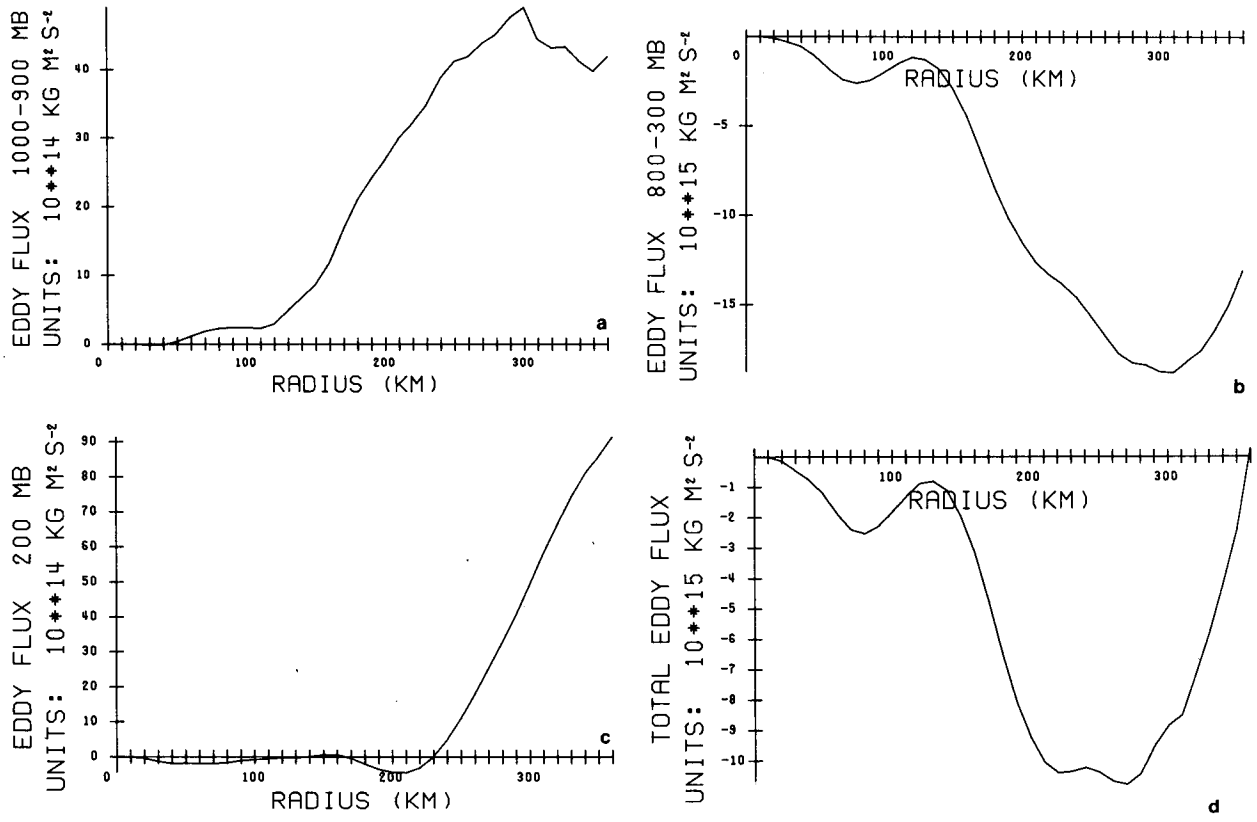

FIG. 21. Contribution of the eddy lateral flux term to the time change of momentum (kg m^2 s^{-2}) plotted as a function of radius for (a) 1000–900 mb; (b) 800–300 mb; (c) 200 mb; and (d) total vertical integral.

The results presented here indicate that assimilation of remotely-sensed heating rates can produce realistic development of mass and wind fields compared to a control integration, and maintain the improvement in the subsequent forecast. It is unlikely, however, that such heating can produce significant changes in the large-scale steering flow over the 12-h period. The feedback of the heating pattern on the large scale is slower and weaker than the forcing in the opposite direction. As a result, the proposed initialization procedure cannot reverse occasional spectacular numerical model failures, such as those producing 500 km or greater position errors in 24 h. Such failures are due to large errors in initial winds, usually in data-poor regions. In regions closer to land, however, such as the Gulf of Mexico, initial data are better and forecast errors are smaller (Neumann and Pelissier, 1981). In such regions, assimilation of observed heating rates can produce useful improvements in hurricane track and intensity predictions over 12–24 h. Such improvements would be of greatest use in the period prior to landfall, when accurate prediction is most vital. Recently, Fiorino and Warner (1981) supplied further evidence of the potential of the procedure with a superior 12 h hurricane intensity forecast on a 60 km mesh using purely satellite-derived rainfall rates.

A long-term goal of this and similar studies is to utilize primitive equation models, which in principle are the best tool, for accurate short-term prediction of both position and intensity of hurricanes, within the time and initial data constraints present operationally. Although caution must be exercised in interpretation of a single case study, the results presented here indicate that incorporation of remotely-sensed rainfall into numerical prediction models can contribute toward this goal.

Acknowledgments. The author expresses his appreciation to Professor T. N. Krishnamurti for his advice and support during the course of this work. Acknowledgment is also extended to H. L. Pan, R. Pasch and M. Kanamitsu for helpful discussions and suggestions, and to D. Jorgenson, B. Lewis and R. Sheets of the National Hurricane Research Laboratory for their help in obtaining data. The author was aided in interpretation of results by an unpublished manuscript of J. B. Hovermale. Thanks are due to Kathy Stutsrim for her careful typing of the manuscript.

This research was supported in its initial and final stages by NOAA Grants 03-4-022-9 and NA80RAC00089, respectively, and for the remainder by NSF Grant ATM-7819363. Computational

support was provided by the Florida State University Computing Center and by the National Center for Atmospheric Research, which is sponsored by the National Science Foundation.

APPENDIX

List of Symbols

A	area
c_x	speed of motion of the computational region in the x-direction
c_y	speed of motion of the computational region in the y-direction
C_D	surface drag coefficient
C_p	specific heat for air at constant pressure
f	Coriolis parameter
g	acceleration of gravity
H_L	heating rate due to condensation
H_R	heating rate due to infrared radiation
i	index for east–west line
j	index for north–south line
k	index for pressure level
L	latent heat of condensation
M	total relative angular momentum in a cylindrical volume
p	pressure
p_b	pressure at cloud base
p_t	pressure at cloud top
P	precipitation rate
q	specific humidity
Q	diabatic heating rate per unit mass
R	universal gas constant
r	radius
t	time
T	temperature
u	east–west velocity component
v	north–south velocity component
v_n	normal velocity component
v_r	radial velocity component
v_λ	tangential velocity component
w	vertical velocity in the z-system
w_k	percentage heating in layer k
x	east–west coordinate
y	north–south coordinate
z	height of a pressure surface
Z	radar reflectivity
α	vertical distribution function for heating
β	df/dy
∇	two-dimensional derivative operator on a pressure surface
ϵ	parameter for adjusting boundary wind components
λ	azimuthal coordinate
ρ	density
ψ	streamfunction
θ	potential temperature
τ	surface stress
ν	coefficient for horizontal diffusion
ω	vertical p-velocity
$(\ )_0$	1000 mb value
$(\ )_b$	value at boundary layer top.

REFERENCES

Anthes, R. A., 1971: A numerical model of the slowly varying tropical cyclone in isentropic coordinates. *Mon. Wea. Rev.*, **99,** 617–635.

——, 1974a: The dynamics and energetics of mature tropical cyclones. *Rev. Geophys. Space Phys.*, **12,** 495–522.

——, 1974b: Data assimilation and initialization of hurricane prediction models. *J. Atmos. Sci.*, **31,** 702–719.

Black, P. G., and R. A. Anthes, 1971: On the asymmetric structure of the tropical cyclone outflow layer. *J. Atmos. Sci.*, **28,** 1348–1366.

Fett, R. W., and S. Brand, 1975: Tropical cyclone movement forecasts based on observations from satellites. *J. Appl. Meteor.*, **14,** 452–465.

Fiorino, M., and T. Warner, 1981: Incorporating surface winds and rainfall rates into the initialization of a mesoscale hurricane model. *Mon. Wea. Rev.*, **109,** 1914–1929.

Frank, W. M., 1977: The structure and energetics of the tropical cyclone II. Dynamics and energetics. *Mon. Wea. Rev.*, **105,** 1136–1150.

Grammeltvedt, A., 1969: A survey of finite difference schemes for the primitive equations for a barotropic fluid. *Mon. Wea. Rev.*, **97,** 384–404.

Griffith, C. G., W. L. Woodley, P. G. Grube, D. W. Martin, J. Stout and D. N. Sikdar, 1978: Rain estimation from geosynchronous satellite imagery—visible and infrared studies. *Mon. Wea. Rev.*, **106,** 1153–1171.

Hoke, J. E., 1976: Initialization of models for numerical weather prediction by a dynamic-initialization technique. Ph.D. thesis, Dept. Meteor., Pennsylvania State University, 118 pp.

——, and R. A. Anthes, 1977: Dynamic initialization of a three-dimensional primitive equation model of Hurricane Alma. *Mon. Wea. Rev.*, **105,** 1266–1280.

Jordan, C. L., 1958: Mean soundings for the West Indies area. *J. Meteor.*, **15,** 91–97.

Jorgenson, D., B. Lewis and R. Trotter, 1978: The precipitation structure of Hurricane Anita (1977) as revealed by quantized airborne radar. *Preprints 18th Conf. Radar Meteorology*, Atlanta, Amer. Meteor. Soc., 34–39.

Kanamitsu, M., 1975: On numerical prediction over a global tropical belt. Ph.D. thesis, Dept. Meteor., Florida State University, 282 pp.

Koss, W. J., 1976: Linear stability analysis of CISK-induced disturbances: Fourier component eigenvalue analysis. *J. Atmos. Sci.*, **33,** 1195–1222.

Krishnamurti, T. N., 1969: An experiment on numerical weather prediction in equatorial latitudes. *Quart. J. Roy. Meteor. Soc.*, **95,** 594–620.

——, M. Kanamitsu, B. Ceselski and M. B. Mathur, 1973: Florida State University's tropical prediction model. *Tellus*, **25,** 523–535.

Lawrence, M. B., 1978: Atlantic hurricane season of 1977. *Mon. Wea. Rev.*, **106,** 534–545.

Matsuno, T., 1966: A finite difference scheme for time integrations of oscillatory equations with second order accuracy and sharp cut-off for high frequencies. *J. Meteor. Soc. Japan*, **44,** 85–88.

Molinari, J., 1979: Numerical simulation of hurricanes using radar and satellite-derived rainfall. Ph.D. thesis, Dept. Meteor., Florida State University, 132 pp.

Neumann, C. J., and J. M. Pelissier, 1981: An analysis of Atlantic tropical cyclone forecast errors, 1970–1979. *Mon. Wea. Rev.*, **109,** 1248–1266.

Ooyama, K. V., 1969: Numerical simulation of the life cycle of tropical cyclones. *J. Atmos. Sci.*, **26,** 3–40.

Palmén, E., and H. Riehl, 1957: Budget of angular momentum and energy in tropical cyclones. *J. Meteor.*, **14,** 150–159.

Pfeffer, R. L., 1958: Concerning the mechanism of hurricanes. *J. Meteor.*, **15,** 113–120.

——, and M. Challa, 1981: A numerical study of the role of eddy fluxes of momentum in the development of Atlantic hurricanes. *J. Atmos. Sci.*, **38,** 2393–2398.

Rodgers, E., R. C. Gentry, W. Shenk and V. Oliver, 1979: The benefits of using short-interval satellite images to derive winds for tropical cyclones. *Mon. Wea. Rev.*, **107,** 575–584.

Rosenthal, S. L., 1970: A circularly symmetric primitive equation model of tropical cyclone development containing an explicit water vapor cycle. *Mon. Wea. Rev.*, **98,** 643–663.

——, 1971: The response of a tropical cyclone model to variations in boundary layer parameters, initial conditions, lateral boundary conditions, and domain size. *Mon. Wea. Rev.*, **99,** 767–777.

Sheets, R. C., 1969: Some mean hurricane soundings. *J. Appl. Meteor.*, **8,** 134–146.

Shuman, F. G., and L. W. Vanderman, 1966: Difference system and boundary conditions for the primitive equation barotropic forecast. *Mon. Wea. Rev.*, **5,** 329–335.

Sundqvist, H., 1970: Numerical simulation of the development of tropical cyclones with a ten-level model. Part I. *Tellus*, **22,** 359–390.

Syono, S., and M. Yamasaki, 1966: Stability of symmetrical motions driven by latent heat release by cumulus convection under the existence of surface friction. *J. Meteor. Soc. Japan*, **44,** 353–375.

Washington, W. M., 1964: Numerical experiments on geostrophic adjustment in a simple fluid system. *Tellus*, **16,** 530–534.

Willis, P. T., and J. F. Spahn, 1977: Z–R relations from drop size measurements in Hurricane Eloise on 22 September 1975. *Proc. 11th Tech. Conf. Hurricanes and Tropical Meteorology*, Miami Beach, Amer. Meteor. Soc., 227–231.

Yamasaki, M., 1968: Detailed analysis of a tropical cyclone simulated with a 13-layer model. *Pap. Meteor. Geophys.*, **19,** 559–585.